PAPER

Electronic and crystal structures of LnFeAsO$_{1-x}$H$_x$ (Ln = La, Sm) studied by x-ray absorption spectroscopy, x-ray emission spectroscopy, and x-ray diffraction (part I: carrier-doping dependence)

View the article online for updates and enhancements.

Electronic and crystal structures of *Ln*FeAsO$_{1-x}$H$_x$ (*Ln* = La, Sm) studied by x-ray absorption spectroscopy, x-ray emission spectroscopy, and x-ray diffraction (part I: carrier-doping dependence)

Yoshiya Yamamoto[1,12], Hitoshi Yamaoka[2,*], Takayuki Uozumi[3],
Atsushi Hariki[3], Seiichiro Onari[4], Jun-ichi Yamaura[5], Kenji Ishii[6],
Takuma Kawai[1], Masahiro Yoshida[1], Munetaka Taguchi[7],
Kensuke Kobayashi[8], Jung-Fu Lin[9], Nozomu Hiraoka[10], Hirofumi Ishii[10],
Ku-Ding Tsuei[10], Hiroshi Okanishi[11], Soshi Iimura[11], Satoru Matsuishi[11],
Hideo Hosono[5,11] and Jun'ichiro Mizuki[1]

[1] Graduate School of Science and Technology, Kwansei Gakuin University, Sanda, Hyogo 669-1337, Japan
[2] RIKEN SPring-8 Center, Sayo, Hyogo 679-5148, Japan
[3] Department of Physics and electronics, Osaka Prefecture University, 1-1 Gakuen, Nakaku, Sakai, Osaka 599-8531, Japan
[4] Department of Physics, Nagoya University, Chikusa, Nagoya 464-8602, Japan
[5] Materials Research Center for Element Strategy, Tokyo Institute of Technology, Yokohama, Kanagawa 226-8503, Japan
[6] Synchrotron Radiation Research Center, National Institutes for Quantum and Radiological Science and Technology, Hyogo 679-5148, Japan
[7] Toshiba Nanoanalysis Corporation, Kawasaki, Kanagawa 212-8583, Japan
[8] Institute of Materials Structure Science, High Energy Accelerator Research Organization (KEK), Tsukuba, Ibaraki 305-0801, Japan
[9] Department of Geological Sciences, The University of Texas at Austin, Austin, Texas 78712, United States of America
[10] National Synchrotron Radiation Research Center, Hsinchu 30076, Taiwan
[11] Laboratory for Materials and Structures, Tokyo Institute of Technology, Yokohama 226-8503, Japan

E-mail: yamaoka@spring8.or.jp

CrossMark

Abstract

A carrier doping by a hydrogen substitution in LaFeAsO$_{1-x}$H$_x$ is known to cause two superconducting (SC) domes with the magnetic order at both end sides of the doping. In contrast, SmFeAsO$_{1-x}$H$_x$ has a similar phase diagram but shows single SC dome. Here, we investigated the electronic and crystal structures for iron oxynitride *Ln*FeAsO$_{1-x}$H$_x$ (*Ln* = La, Sm) with the range of $x = 0$–0.5 by using x-ray absorption spectroscopy, x-ray emission spectroscopy, and x-ray diffraction. For both compounds, we observed that the pre-edge peaks of x-ray absorption spectra near the Fe-*K* edge were reduced in intensity on doping. The

---

*Author to whom any correspondence should be addressed.
[12] Present address: Nagoya Institute of Technology, Gokiso, Showa, Nagoya, Aichi 466-8555, Japan.

character arises from the weaker As–Fe hybridization with the longer As–Fe distance in the higher doped region. We can reproduce the spectra near the Fe-K edge according to the Anderson impurity model with realistic valence structures using the local-density approximation (LDA) plus dynamical mean-field theory (DMFT). For $Ln =$ Sm, the integrated-absolute difference (IAD) analysis from x-ray Fe-$K\beta$ emission spectra increases significantly. This is attributed to the enhancement of magnetic moment of Fe $3d$ electrons stemming from the localized picture in the higher doped region. A theoretical simulation implementing the self-consistent vertex-correction method reveals that the single dome superconducting phase for $Ln =$ Sm arises from a better nesting condition in comparison with $Ln =$ La.

S Supplementary material for this article is available online

(Some figures may appear in colour only in the online journal)

1. Introduction

Since the discovery of iron-based superconductors [1], various types of structural series have been reported [2]. The '1111' series, LnFeAsO ($Ln =$ lanthanide), is the prototype iron-based superconductor, which has a ZrCuSiAs-type structure with alternating stacks of conducting FeAs$_4$ units and charge reserver (O, H)La$_4$ layers [2]. The non-doped LnFeAsO involves tetragonal to orthorhombic structural transitions at 120–160 K followed by a paramagnetic (PM) to antiferromagnetic (AFM) transition. We call the magnetic ordered state with the orthorhombic structure as the parent phase. As a result of doping the electron by O^{2-} substitution to the F$^-$ ($x < 0.2$), the superconducting (SC) state emerges in place of the magnetic and orthorhombic structural phases. An advanced doping method with the dopant (H$^-$) surpassed the doping limit at $x = 0.2$ in 1111 materials and unveiled the bipartite magnetic parent phases at $x \sim 0$ (AFM1) and $x \sim 0.5$ (AFM2) and the two superconducting (SC) phases with T_c, max $= 26$ K at $x \sim 0.08$ (SC1) and T_c, max $= 36$ K at $x \sim 0.35$ for LaFeAsO$_{1-x}$H$_x$ [3–10]. Different magnetic structures and distinctive magnetic moments for AFM1 and AFM2 were found from the neutron diffraction measurements [8, 11]. LaFeAsO$_{1-x}$H$_x$ and LaFeAsO$_{1-x}$F$_x$ have the same electronic/magnetic phase diagrams [1, 4]. Since the distinctive magnetic parent phases of AFM1 and AFM2 adjacent to the respective SC1 and SC2, we consider that the origin of superconductivities should come from different mechanisms. The AFM quantum criticality is also observed near $x \sim 0.5$ from NMR study [12]. In the iron-based superconductors, theoretical works have been proposed that the paring mechanism of superconductivity is mediated by the fluctuations of the spin density wave (SDW) due to the Fermi surfaces (FS) nesting [13, 14]. Another theoretical work using the self-consistent

vertex–correction (SC-VC) method proposed that the spin + orbital fluctuation drives the superconductivity [15–19].

Unlike to $Ln =$ La, SmFeAsO$_{1-x}$H$_x$ exhibits a single SC phase with holding two magnetic parent phases [20–22]. The magnetic moments was determined to be $0.66\mu_B$/Fe at $x = 0$ (AFM1) and $2.73\mu_B$/Fe at $x = 0.73$ (AFM2). The normal state resistivity implies that $Ln =$ La is regarded as a Fermi liquid in the lower doped region and a non-Fermi liquid in the higher doped region, whereas $Ln =$ Sm behaves a non-Fermi liquid character in resistivity over the entire doped region. Concerning the distinctive character of the SC dome and the normal state resistivity between $Ln =$ La and Sm, one might expect to the different nesting condition for both compounds. Moreover, a local or itinerant picture of Fe spin state should be elucidated because the embedding the Fe magnetic moment, formed by the local Hund's coupling into metallic host with itinerant As $4p$ states, gives rise to an anomalous metal–Hund's metal–with the non-Fermi liquid character. The origin of superconductivity remains a controversial subject albeit the tremendous efforts in this system thus far; thereby the further investigation on the microscopic electronic states is required.

In this paper, we examined electronic and crystal structures for LnFeAsO$_{1-x}$H$_x$ ($Ln =$ La and Sm) over the entire doping range of x using x-ray emission spectroscopy (XES), high-resolution x-ray absorption spectroscopy (XAS), and x-ray diffraction (XRD). Based on high-resolution XAS measured by the partial-fluorescence yield mode (PFY-XAS) [23, 24] at the Fe K- and As K-edges, we can analyze the change of Fe $3d$ states and the hybridization of Fe and As $4p$ states on doping as discussed in literature [25, 26]. Moreover, we calculated the PFY-XAS spectra at Fe K-edge based on the Anderson impurity model (AIM) combined with the DFT band structure. The Fe $K\beta$ XES measurement is a state of the art method to probe the local Fe spin state [27, 28]. Additionally, we discuss

the difference in the nesting condition for $Ln =$ La and Sm using the SC-VC approach. At each section we will provide a comparison between LaFeAsO$_{1-x}$H$_x$ and SmFeAsO$_{1-x}$H$_x$ systems.

2. Experiments and methods

Polycrystals of LaFeAsO$_{1-x}$H$_x$ ($x =$ 0, 0.07, 0.14, 0.25, 0.35, 0.4, 0.49, and 0.51) and SmFeAsO$_{1-x}$H$_x$ ($x =$ 0, 0.22, 0.59, and 0.65) were prepared by the high-pressure method as reported in the literature [4]. All the spectroscopy and diffraction measurements were performed at BL11XU and BL12XU, SPring-8 using the undulator beam monochromatized by a cryogenically-cooled double crystal Si(111) monochromator [27, 29]. A channel-cut Si(400) monochromator was also used after the double crystal monochromator at BL11XU. Johann-type spectrometers were equipped with a spherically bent Si(531) analyzer of radius of $\sim$1 m for Fe $K\beta$ emission and Si(844) for As $K\beta$ emission at BL12XU and three-diced and bent Ge(620) analyzers of radius of $\sim$2 m for Fe $K\beta$ emission at BL11XU. A Si solid state detector (Amptech) and a PILATUS area detector [30] were used to analyze the Fe emission of the $3p \rightarrow 1s$ de-excitation at the Fe and As K-absorption edges. The PILATUS detector has an advantage to reduce the background and can measure higher count rate compared to the other detectors such as a SSD and a scintillation counter. For the PFY-XAS spectra, As $K\beta$ emission was employed instead of the $K\alpha$ emission [25, 26] because the As $3p$ electrons are prone to the outer shell electrons in comparison with the $2p$ electrons. At the emitted photon energy of 7.6 keV the overall energy resolution was set to be 0.9 eV at BL12XU and 1.2 eV at BL11XU. The intensities of the spectra were normalized by those of the incident beam. The incident photon flux was measured to be on the order of 1.0×10^{13} photons s^{-1} at 7.1 keV and 1.3×10^{13} photons/s at 11.8 keV at BL12XU by a pin diode detector. After a Kirkpatrick–Baez (K–B) mirror, they were reduced to be 50%–60% of the intensity. The photon flux was estimated to be 7×10^{12} photons s^{-1} at 7.1 keV at BL11XU. The errors of the intensity and energy of each component of the PFY-XAS spectrum come from the statistical errors of the total counts and the fit errors.

Fe $K\beta$ emission spectra involves a main $K\beta_{1,3}$ and a weak satellite of $K\beta'$ components. The relative intensity of the $K\beta'$ peak is a measure of the spin state [31, 32]. The integrated-absolute difference (IAD) based on a reference material FeCrAs [28] in the Fe $K\beta$ emission spectra exhibits closely correlation to the spin state of d electrons and the magnetic moment [33, 34].

The IAD analysis was performed in the following way [35]: (i) match the center of mass spectra between the sample and reference exactly after extracting the background, (ii) take difference between them, (iii) integrate the absolute value of the difference. The intensity was normalized by the area of the $K\beta$ spectrum. The error of IAD represents the statistical error of the total counts. The XRD measurements were carried out for $Ln =$ La at $x =$ 0, 0.07, 0.35, and 0.51 and $Ln =$ Sm at $x =$ 0, 0.22, and 0.65 at SPring-8 BL12B2 equipped with a CCD area detector at room temperature. 2D images were integrated to

yield 2θ-intensity data on FIT2D program [36]. The crystal structures were determined using the Rietveld method on the RIETAN-FP program [37, 38].

3. Results and discussion

3.1. PFY-XAS

Figures 1(a) and (b) display the PFY-XAS spectra and its expanded view near the pre-edge around the Fe-K absorption edge for LaFeAsO$_{1-x}$H$_x$ at room temperature and ambient pressure. The pre-edge peak on PFY-XAS spectrum satisfies the sum of the electric dipole and quadrupole intensities, where the Fe $4p$ character is mixed into the Fe $3d$ orbitals due to the loss of inversion symmetry locally on the tetra-coordination of Fe. The intensity of the pre-edge peak diminishes with doping the electron, i.e. the increase of x, as shown in figure 1(b). We consider that the observation arises from the decrease of the Fe($3d$)–As($4p$) hybridization with the elongation of As–Fe distance on doping. Moreover, the position of pre-edge peak shifts to low energy side on doping; this is explained as a result that the doped electron fills the empty states of Fe d orbitals. Figure 1(c) exhibits the deconvolution of PFY-XAS spectra based on the Voigt function with an arctan-like background. Two components, P1a and P1b, were required to fit the pre-edge peak [35, 39]. Figure 1(d) presents the x dependence of the intensity and the energy for P1 peak (P1 = P1a + P1b), which exhibits suddenly reductions above $x = 0.4$ at around the vanishing point of SC2. Since the narrow $3d_{xy}$ band is regarded as the half-filled regime in the higher doped region [9], the above findings are related to a strong depression of the coherent scale arising from the increase of effective Coulomb repulsion. We will discuss the source of the P1 peak shift from the theoretical calculation in the subsequent subsection.

Figures 1(e), (f), (h), and (i) give the PFY-XAS spectra and their expanded view at the Fe-K and As-K absorption edges for $Ln =$ Sm, respectively. We observed the decrease of intensity and the lower shift of relative energy of the pre-edge peak on doping, as demonstrated in figure 1(g). As described in the above for $Ln =$ La, the findings arise from the decrease of the Fe($3d$)–As($4p$) hybridization and the introduction of electron to the empty states of Fe d orbitals toward the higher doped region.

In both LaFeAsO$_{1-x}$H$_x$ and SmFeAsO$_{1-x}$H$_x$, the absorption edge of the PFY-XAS spectra at the Fe-K edge shifted slightly to the lower energy with x. The Fe–As bond length increased with the electron doping as shown below. This indicates that the Fe valence decreases with the electron doping, resulting in the weaker covalency. The intensity of P1a decreased rapidly with x, while that of P1b increased slightly. [35] Thus, the hydrogen substitution to the oxygen site causes the electron carrier doping to the Fe d band, resulting in the decrease of the total intensity of the pre-edge peak.

Figure 1(j) exhibits the deconvolution of As-K PFY-XAS spectra, where the P4, P5, and P6 peaks correspond to the density of states (DOS) of As p states [25]. We found the intensity decrease and the relative energy shift of the P4 pre-
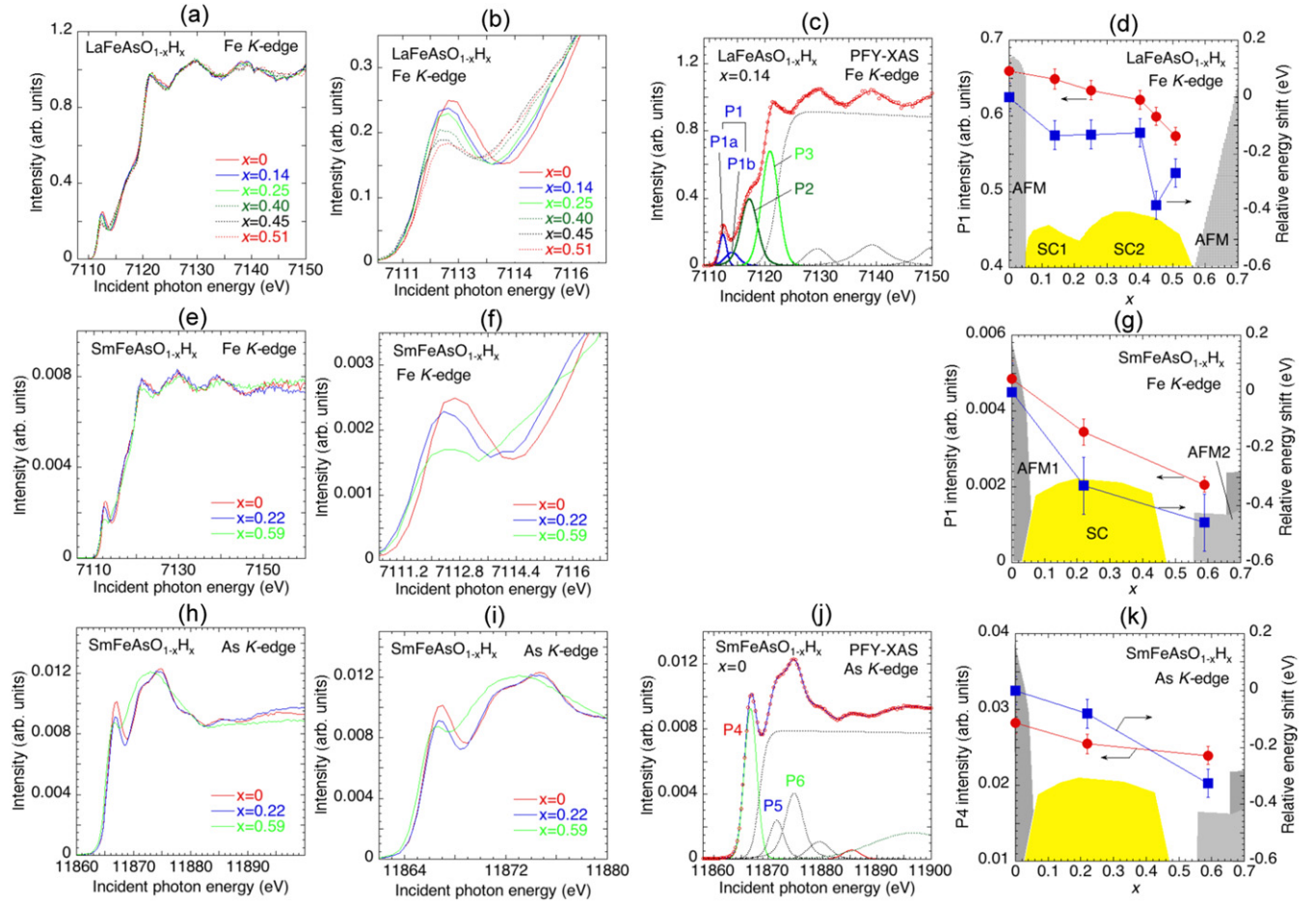
Figure 1. Carrier doping dependence of the PFY-XAS spectra for LaFeAsO$_{1-x}$H$_x$ and SmFeAsO$_{1-x}$H$_x$ at room temperature and ambient pressure. (a) and (e) PFY-XAS spectra at the Fe-*K* absorption edge. (b) and (f) Expanded views of the PFY-XAS spectra around the pre-edge peak. (c) A fit example of the PFY-XAS spectrum at the Fe-*K* absorption edge. (d) and (g) The intensity and relative energy shift of the P1 peak of the PFY-XAS spectra at the Fe-*K* absorption edge (h) PFY-XAS spectra at the As-*K* absorption edge. (i) Expanded view of the PFY-XAS spectra around the As-*K* absorption edge. (j) A fit example of the PFY-XAS spectrum at the As-*K* absorption edge. (k) Relative energy shift of the P4 peak at the As-*K* absorption edge. Grey- and yellow-colored areas in (d), (g), and (k) correspond to the AFM and superconducting regions, respectively, where the maximum value of the vertical axis scales to be 150 K in (d) [20, 22] and 100 K in (g) and (k) [40–43]. The dark and light gray areas in figures 1(g) and (k) represent the AFM phases determined from the measurements of heat capacity and power neutron diffraction, respectively [22].

peak, as demonstrated in figure 1(k). The spectral feature at $x = 0.59$ at the As-*K* absorption edge was very different from others and the absorption edge shifted to the lower energy at $x = 0.59$ as shown in figure 1(i). It is interesting to clarify the fact that these results are coincident with the disappearance of the superconductivity at $x = 0.59$ in SmFeAsO$_{1-x}$H$_x$.

3.2. *Kβ* XES

Figures 2(a) and (e) show the Fe $K\beta$ XES spectra for $Ln =$ La and Sm, respectively. Figures 2(b) and (f) plot the relative intensity estimated by subtracting the reference FeCrAs from the data for the respective La and Sm. Figures 2(c) and (g) are expanded view around a peak of the Fe $K\beta$ XES spectra for the respective La and Sm. Figures 2(d) and (h) display the IAD values estimated by the integration of the relative intensity for the respective La and Sm. Figures 2(d) and (h) for the respective La and Sm illustrate the IAD values and the magnetic moments

estimated from the corresponding IADs as discussed in literature [33, 34]. The IAD values for $Ln =$ La were insensitive to x except $x = 0.25$, while the IAD values for $Ln =$ Sm gained its intensity at $x = 0.59$. Looking at it from a different viewpoint, the magnetic moment became larger where T_c becomes lower at $x = 0.25$ for La and the superconductivity disappears for Sm. We checked the temperature dependence of the IAD values of for La at $x = 0, 0.35, 0.51$, and 0.62 (the data are not shown here); however, no significant changes were observed within the experimental errors.

The neutron diffraction measurements have indicated the magnetic ordered moment of 0.63 ($x = 0$) and $1.21\mu_B$/Fe ($x = 0.51$) for $Ln =$ La, and 0.66 ($x = 0$), 0.77 ($x = 0.56$), and $2.77\mu_B$/Fe ($x = 0.73$) for $Ln =$ Sm [8, 11, 22, 44]. The IAD values in the low-doping range give the magnetic moment of $0.50\mu_B$ ($x = 0$) for La, and 0.78 ($x = 0$) and $1.35\mu_B$ ($x = 0.59$) for Sm, which agrees with the neutron data. However, the magnetic moments from IAD deviated from the
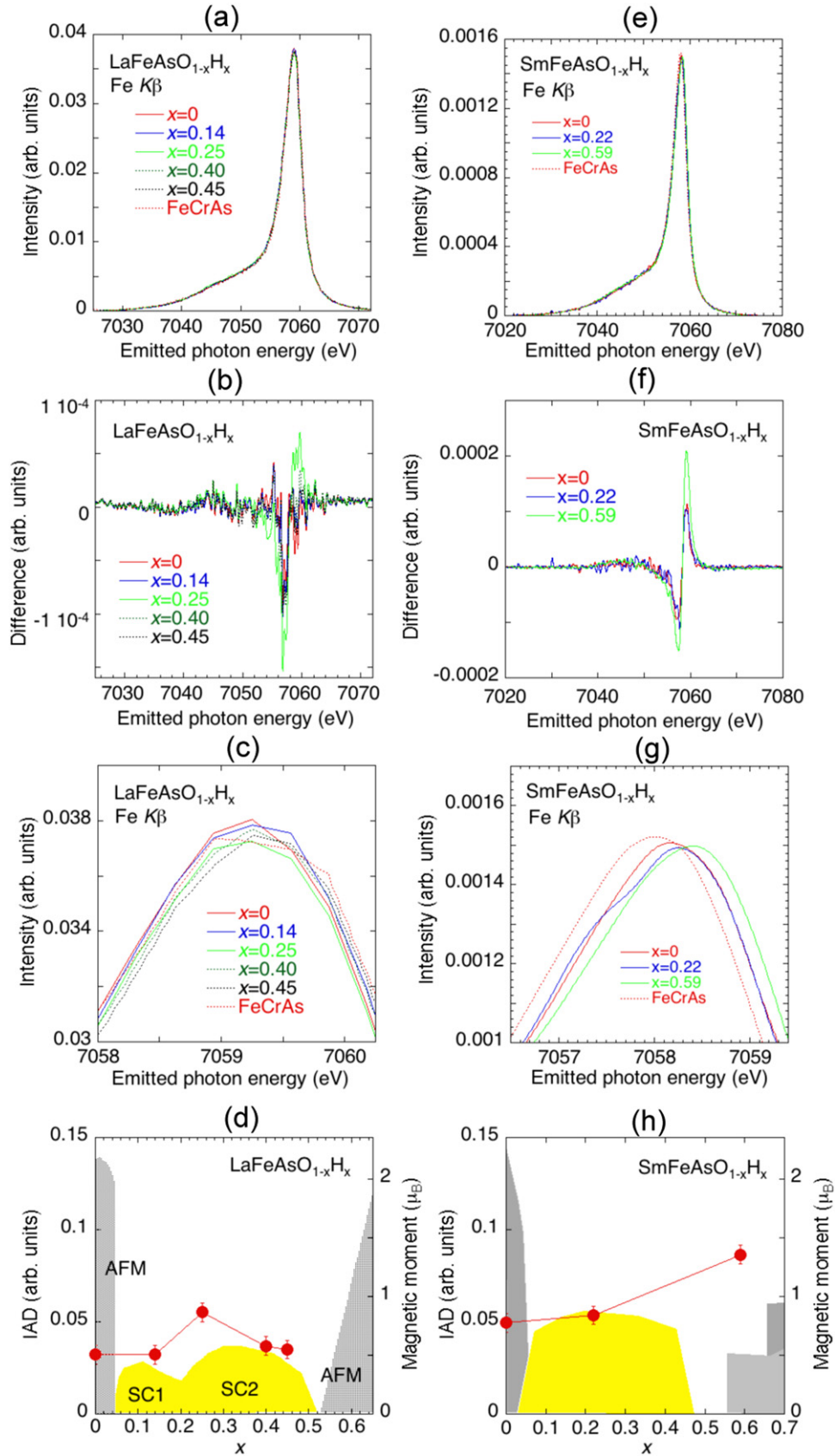
Figure 2. (a) and (e) Carrier doping dependence of the Fe Kβ XES spectra for LaFeAsO$_{1-x}$H$_x$ and SmFeAsO$_{1-x}$H$_x$, respectively. (b) and (f) Differences of the intensity of the spectra for the spectrum of FeCrAs. (c) and (g) Expanded views around the peaks in (a) and (e). (d) and (h) IAD values with the magnetic moment [28, 33]. Grey- and yellow-colored areas in (d) and (h) correspond to the AFM and superconducting regions, respectively, where the maximum value of the vertical axis scales to be 150 K in (d) [20, 22] and 100 K in (h) [40–43].
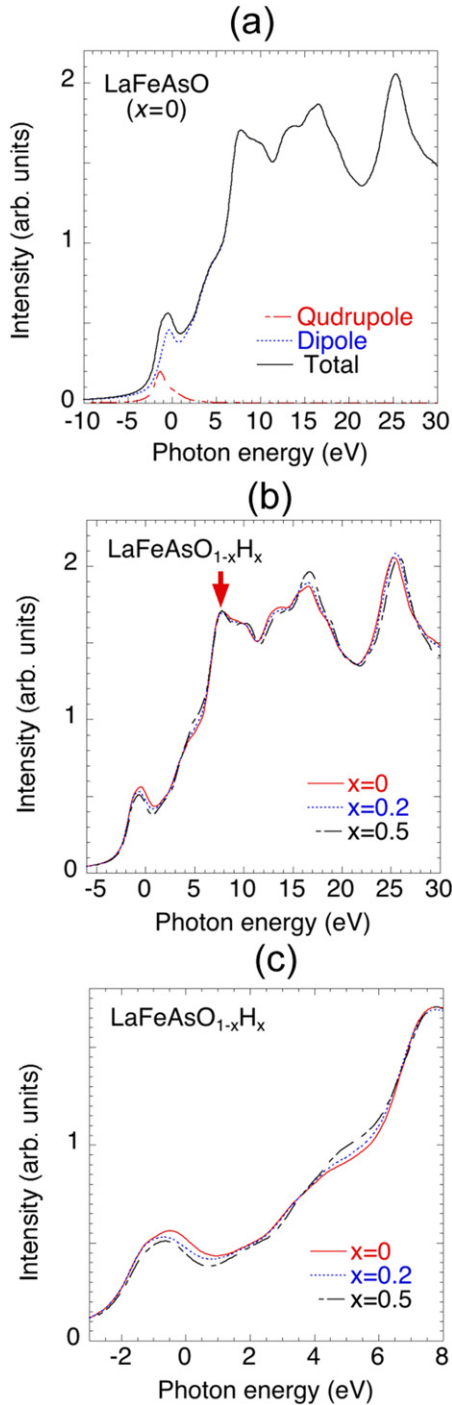
Figure 3. Results of the impurity Anderson model calculations of the PFY-XAS spectra at Fe-*K* absorption edge. (a) *K*-XAS spectra (black solid line) for $x = 0.0$ with the DT (blue dotted line) and the QT (red dashed line). (b) *K*-XAS for $x = 0$ (red solid line), 0.20 (blue dotted) and 0.51 (black dashed line). The relative photon energy positions of the calculated spectra are aligned so that the absorption edges become the same energy position indicated by the red arrow. (c) Expanded view of (b) near the pre-edge peak and absorption edge.

neutron data in the higher doped region for both La and Sm.

The magnetic moments from the inelastic neutron scattering, XES, and photoelectron spectroscopy are prone to be higher than those from neutron diffraction, NMR, μSR, and Mössbauer methods [45]. Our results, however, indicate lower magnetic moments in higher x in comparison with the neutron diffraction [8, 11, 22]. The origin of the satellite, $K\beta'$ of the $K\beta_{1,3}$ spectrum, is mainly considered as the exchange interaction between $3p$ hole and $3d$ electron. [33] The intensity of $K\beta'$ may be weakened with the mixing of the $3d$ orbitals. Here, we propose a possible scenario for explaining the deviation between the different measurements: since XES probes the localized magnetic moment on the atom, it is insensitive to detect the valence itinerant electrons contributing the spin moment above AFM, where the IAD is considered to give the minimum value of the magnetic moment [45, 46]. Moreover, the neutron diffraction measurement was carried out below the $T_{\rm N}$ in contrast to our measurement above $T_{\rm N}$. We thus suggest that the neutron diffraction results assess the magnetic moment of the localized- plus itinerant-components, and IAD assesses only the localized magnetic moment.

The band calculations for $Ln = {\rm La}$ indicated the strong FS nesting between the electron and hole bands in the lower doped region and the weak FS nesting in the higher doped region [4]. The orbital fluctuation caused by the d band degeneration was dominant because the energy of the anti-d_{xy} orbital decreased with x and those of anti-d_{xy}, $d_{yz,zz}$, and d_{xy} matched each other around $x = 0.36$ [4]. Ion radius of Sm ion is smaller than that of La ion, and as a consequence of this in LaFeAsO$_{1-x}$H$_x$ the crystal structure is deviated from the regular tetrahedron crystal structure as shown below, while in SmFeAsO$_{1-x}$H$_x$ locates near the ideal regular tetrahedron crystal structure. Thus, in SmFeAsO$_{1-x}$H$_x$ the energy difference among the d orbitals is small, so the orbital fluctuation which may lead to the single dome superconductivity is enhanced. As will be described later, the shape of FeAs$_4$ in the SC region deviates from the regular tetrahedron for $Ln = {\rm La}$ and it approaches the regular one for $Ln = {\rm Sm}$. Accordingly, we infer that the Fe d bands are nearly degenerate for $Ln = {\rm Sm}$ with the higher-$T_{\rm c}$, which reminds us of that the orbital fluctuation mechanism works for the high-$T_{\rm c}$ superconductivity.

The inelastic neutron scattering has pointed that the electron doping enhances the localized picture in $Ln = {\rm La}$ system [47]. Moreover, the d–p hybridization becomes weaker along with the elongation of the As–Fe distance with increasing the x. The higher IAD value at $x = 0.59$ of SmFeAsO$_{1-x}$H$_x$ than those at $x = 0$ and 0.22 in figure 2(h) also suggests the more localized magnet moment at AFM2. We thus infer that the electron doping alters the magnetic character from itinerant to localized nature in the 1111 system.
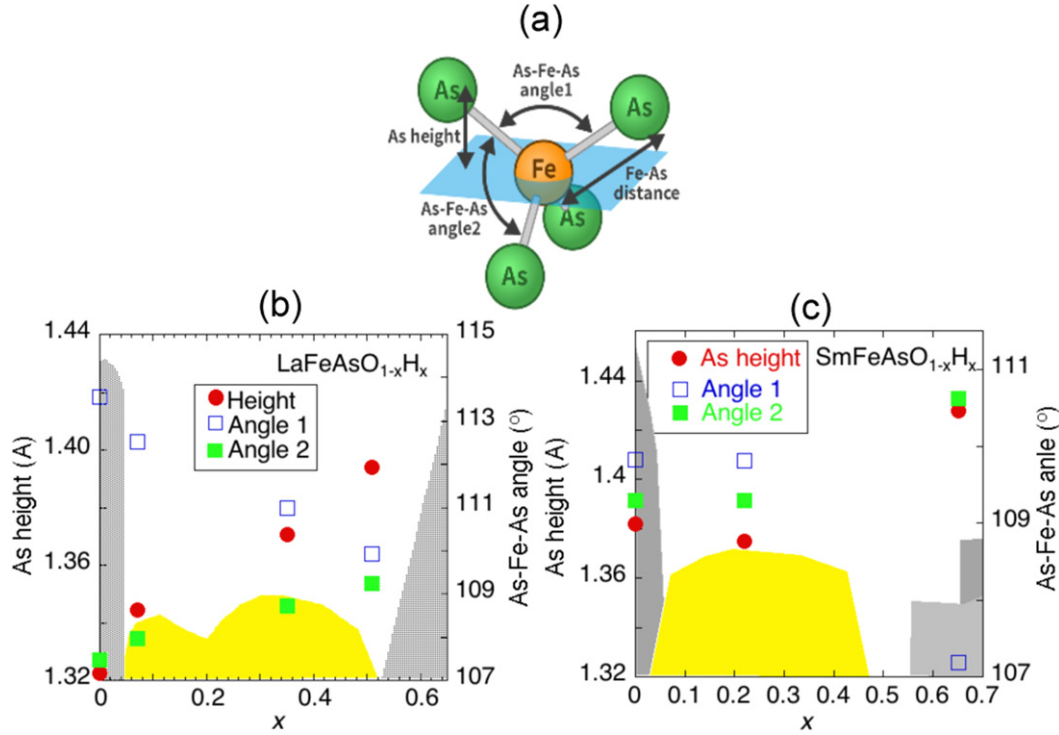
Figure 4. (a) Definition of the As height from the Fe basal plane, the As–Fe distance, and As–Fe–As angles. (b) and (c) Carrier doping dependence of the As height and As–Fe–As angles for LaFeAsO$_{1-x}$H$_x$ and SmFeAsO$_{1-x}$H$_x$, respectively. Grey- and yellow-colored areas in (b) and (c) correspond to the AFM and superconducting regions, respectively, where the maximum value of the vertical axis scales to be 150 K in (b) [20, 22] and 100 K in (c) [40–43].

3.3. Anderson impurity model calculations

To study the PFY-XAS features at the Fe *K*-edge, especially the change in the pre-peak with *x*, we perform a theoretical simulation using AIM. The AIM describes the excited Fe site as an impurity which hybridizes with the valence states in the rest of the crystal. The valence states are constructed from the band structure calculation using local-density approximation (LDA) + dynamical mean-field theory (DMFT) [48–51]. In LDA + DMFT, the local distortion of the FeAs$_4$ tetrahedron, which is almost pure T_d symmetry at $x = 0.51$ and D_{2d} symmetry at $x = 0$ for *Ln* = La, was taken into account in the LDA band structures. The LDA bands obtained using *WIEN2k* code [52] are mapped onto a tight-binding model spanning Fe 3*d*, As 4*p*, and O 2*p* states using wien2wannier [53] and wannier90 [54]. Then, the DMFT calculation for the tight-binding model was performed, see details in references [48, 49, 55]. Finally, we compute the Fe *K*-edge spectra using the AIM with the hybridization function which encodes the valence states described in LDA + DMFT. The configuration interaction (CI) solver with the Lanczos algorithm was used to compute the spectral intensities in AIM [49, 50, 55]. The six configurations of d^7, $d^8\underline{v}$, $d^9\underline{v}^2$, d^6c, $d^7\underline{v}c$, $d^8\underline{v}^2c$ are used to represent the ground state, where $\underline{v}$ and c denote a valence hole below Fermi energy E_F and a conduction electron above E_F, respectively. The contribution of the quadrupole transition (QT) was calculated separately from that of the dipole transition (DT). The final state of QT was described by linear combination of configurations of sd^8, $sd^9\underline{L}$, $sd^{10}\underline{v}^2$, sd^7c,

$sd^8\underline{v}c$, $sd^9\underline{v}^2c$ (*s* is an electron in the 1*s* shell). We calculate the DT as the convolution of the Fe 4*p* partial DOS multiplied by the matrix element of optical transition using *WIEN2k* code [52] with the Fe 1*s* XPS calculated by AIM. This treatment of DT [56] is justified by the fact that the main screening channel of the final state in DT is given not by the excited Fe 4*p* electron but by electrons on the surrounding ligands to the Fe 3*d* states because of much weaker 1*s* core-hole potential for the excited 4*p* electron than that for the Fe 3*d* electrons in DT. Then the final state of 1*s* XPS in the DT calculation is described by sd^7, $sd^8\underline{v}$, $sd^9\underline{v}^2$, sd^6c, $sd^7\underline{v}c$, $sd^8\underline{v}^2c$. Note that the local distortion of FeAs$_4$ for the *x* values of 0, 0.20, and 0.51 are taken into account both in the hybridization function of AIM and in the 4*p* partial DOS. The Hubbard *U* and Hund's *J* parameters on the Fe 3*d* shell are taken from reference [57]. The parameters used for the core-valence interactions in AIM can be found in supplementary information (https://stacks.iop.org/JPCM/33/255602/mmedia) [35].

Figure 3(a) shows the *K*-XAS spectrum (black line) calculated by AIM for $x = 0$. The contributions from the DT (blue line) and the QT (red line) are shown together. We find that the spectral features in the experimental data are well reproduced over the entire energy range. Figure 3(b) shows the results calculated for $x = 0$ (red), 0.20 (blue) and 0.51 (black). Here the relative photon energies are aligned to the experimental absorption edges indicated by the arrow. The AIM calculation qualitatively reproduces the shift of the pre-peak to the low-energy side as well as the decrease of its intensity with increasing *x* from 0 to 0.51 observed in the experimental data.
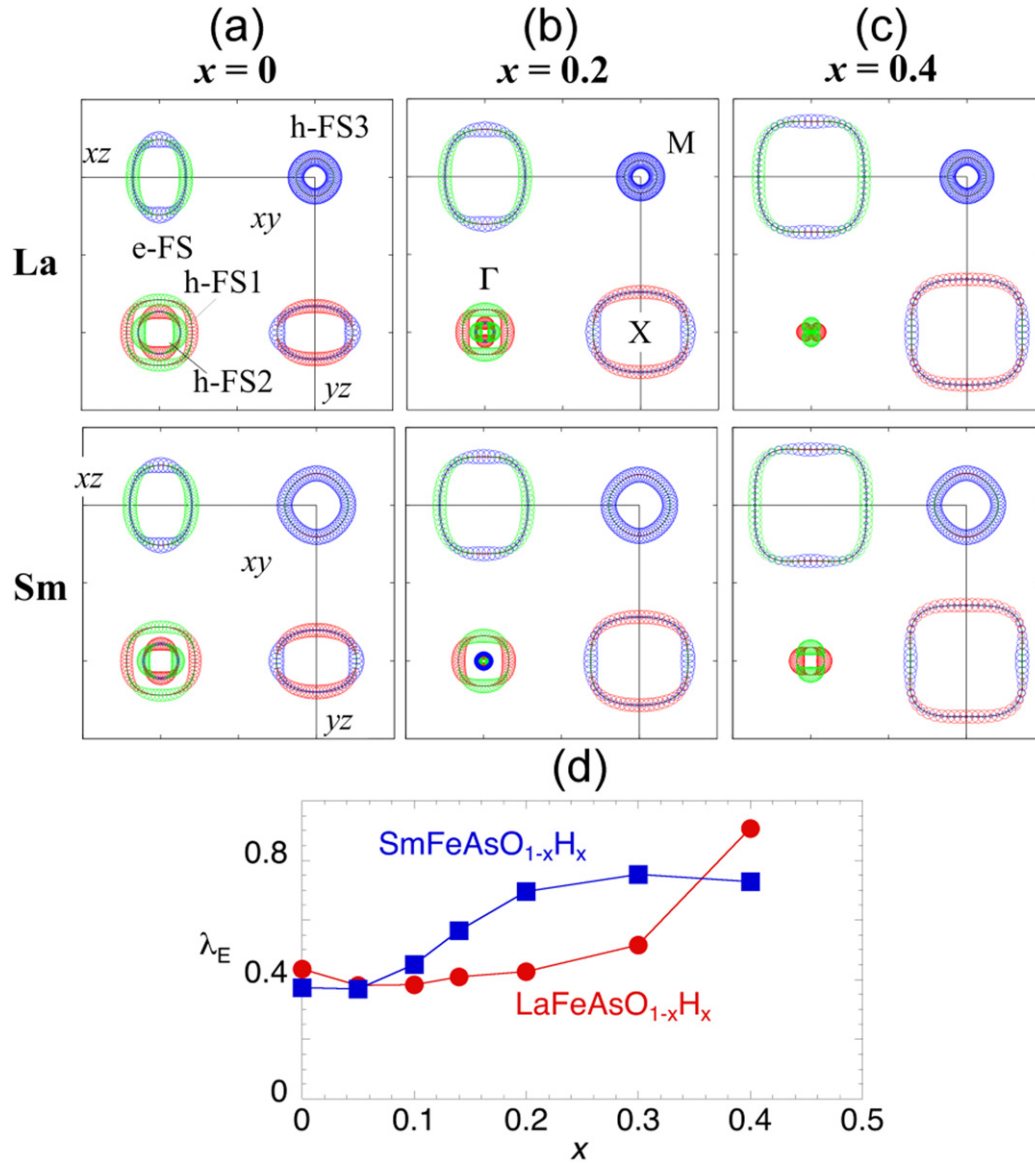
Figure 5. Fermi surface mappings of (a) $x = 0$, (b) $x = 0.2$, and (c) $x = 0.4$ of LaFeAsO$_{1-x}$H$_x$ and SmFeAsO$_{1-x}$H$_x$ obtained by first principles calculations. [35] e-FS and h-FS correspond to electron Fermi surface and hole Fermi surface, respectively. (d) The eigen value of the gap equation (Eliashberg equation) of the superconductivity as a function of x for LaFeAsO$_{1-x}$H$_x$ and SmFeAsO$_{1-x}$H$_x$ [15–19].

Given the reasonable agreement with the experimental data, we discuss the change of the Fe d states with increasing x. The elongation of Fe–As bonds weakens the covalent bonding between the two. With this, one could expect a charge transfer from Fe to As sites, and thus an increase of the Fe K-edge and a decrease of As K-edge absorption intensities. Though the latter is observed in the As K-edge absorption, see figure 1(k) for $Ln =$ Sm, the Fe K-edge XAS results show an opposite trend with x, the intensities decrease for both $Ln =$ La and Sm. The integrated weights in the configurations with $N = 6$, 7, 8 electrons on the Fe $3d$ shell are as follows (%): 16.8, 42.9, 31.4 for $x = 0$; 12.0, 39.0, 37.5 for $x = 0.20$; 7.9, 31.6, 43.6 for $x = 0.51$. Thus, the weights of the configurations with 8 electrons in Fe $3d$ shell increase nearly monotonically with the electron doping (x). The average Fe d electron number is 7.32, 7.43, and 7.70 for $x = 0, 0.20, 0.51$, respectively. Therefore, the

doped electrons mainly go to the empty states of Fe $3d$ states, which overcompensates a possible hole doping from As to Fe sites due to the elongation of Fe–As bonds. Thus, both the Fe and As K-edge absorption intensities can be decreased with the carrier doping x. The discussion above is consistent with the valence structure obtained in LDA + DMFT, see supplementary information [35], showing the low-energy empty states are dominated by Fe $3d$ states. The anti-bonding states with large As $4p$ contributions are pushed to well above E_F due to a large Fe–As hybridization. Thus, a direct electron doping to the As $4p$ states is expected to be rather small.

3.4. Crystal structure

Figure 4 depicts the representative structural parameters via crystal structure analyses. Figure 4(a) signifies the As height from the Fe basal plane, the As–Fe distance, and As–Fe–As

angles that are strongly tied to the electronic structure as discussed in the previous theoretical work [58].

The As height of $Ln = $ La increased with increasing x, as shown in figure 4(b), which agrees well in the literature [59]. As described above, the As–Fe distance increased with the carrier doping and thus it is intuitively understood that the Fe $3d$–As $4p$ hybridization may decrease. [22, 59] The decrease of the hybridization with x was also supported by the band structure calculations [9].

Carrier-doping dependence of the lattice constants agrees well with the previously-measured ones [3, 20, 60, 61] (see the supplementary information [35]). The doping dependence of the As height and As–Fe–As angle of $Ln = $ Sm are shown figure 4(c). Both the As–Fe–As angle and As height at $x = 0.65$ deviate largely from ideal values of an angle of $109.5°$ [62] and a height of ~1.38 Å [63]. This anomaly at $x = 0.65$ corresponds to the change in the PFY-XAS spectra at the As-K absorption edge and the increase of the IAD values at $x = 0.59$. The anomaly of the crystal and electronic structures possibly correlates to the suppression of the superconductivity at $x \sim 0.6$.

An intriguing result of calculation for $Ln = $ Sm was proposed by Iimura *et al* [22] positing that $t_1{}^{d_{xy}}$, which is a nearest-neighbor hopping parameter of the Fe-$3d_{xy}$ orbital, fades away to zero, leading to the enhancement of electron correlation. Our results of SmFeAsO$_{1-x}$D$_x$ showed the very different electronic structure at $x = 0.59$ and support the theory. Such reduction in the $t_1{}^{d_{xy}}$ parameters was attributed to the longer Fe–anion and the shorter Fe–Fe bond lengths, but they showed that the indirect electron doping was more significant than the structural changes. Present results of the electron doping caused the both changes in the crystal and electronic structures: the increase of the As–Fe distance, the decrease of the p–d hybridization, more localized magnet at AFM2. We consider that the calculation agrees with our findings that the decrease of p–d hybridization and the localized picture in the higher doped region.

3.5. Origin of a single dome superconductivity

A small carrier doping may weaken the nesting condition with reducing the spin susceptibility. The carrier doping also suppressed the AFM order in LnFeAsO$_{1-x}$H$_x$. A similar phenomenon has been observed in the electron doping with Co substitution to Fe site in BaFe$_2$As$_2$, where a few % Co substitution suppressed the AFM order and superconductivity appeared [26, 64]. Onari *et al* [15] theoretically suggested that in LaFeAsO$_{1-x}$H$_x$ the anion-height instability was a key factor for high-T_c superconductivity; the C_4 isostructural phase transition at $x \sim 0.5$ changed the anion-height with decreasing the temperature, and the non-nematic O$_{3z^2-r^2}$ order, while the C_2 transition at $x \sim 0$ induced nematic order and did not show a sizable change in the anion-height.

Let us move on the difference of SC domes for $Ln = $ La and Sm. We examined the spin-fluctuation-mediated orbital order based on the SC–VC method for $Ln = $ La and Sm [15]. In the method, the VC for the irreducible charge (orbital) susceptibility was estimated self-consistently. The orbital sus-

ceptibility was enhanced by the interference of the spin fluctuations mainly due to the Aslamazov–Larkin type VC. Figures 5(a)–(c) illustrate the FS mappings for $Ln = $ La and Sm ($x = 0.1$, 0.2, and 0.4), respectively (more-detailed mappings are shown in reference [35]). We found a larger hole-type FS at M point and better nesting condition for $Ln = $ Sm in comparison with $Ln = $ Sm. Figure 5(d) plots the eigen value (λ_E) of the gap equation (Eliashberg equation) of the superconductivity based on s^{++} superconductivity, where λ_E is a measure of T_c [15, 17–19]. The λ_E for $Ln = $ Sm was larger than that for $Ln = $ La, resulting in a single SC dome for $Ln = $ Sm. Suzuki *et al* also reported similar theoretical results; the stable hole Fermi surface is larger for Sm1111 than for La1111 [65].

4. Conclusion

Carrier doping dependence of electronic and crystal structures of LnFeAsO$_{1-x}$H$_x$ ($Ln = $ La, Sm) were studied in detail. For $Ln = $ La and Sm, the intensity of the pre-edge peak at the Fe-K absorption edge decreased with the electron doping while the As–Fe distance increased with decreasing the As–Fe hybridization. The impurity Anderson model reproduced well the experimental spectra at the Fe-K absorption edge. For $Ln = $ Sm the IAD values became large and shifted to higher-spin state at $x = 0.59$, corresponding to the anomaly of the As height and As–Fe–As angle, and this implies more localized nature in magnetism at AFM2. The theory with the SC–VC method suggests the single dome superconductivity in Sm1111 arises from the better nesting condition than the case of La1111.

Data availability statement

All data that support the findings of this study are included within the article (and any supplementary files).

ORCID iDs

Hitoshi Yamaoka ⬤ https://orcid.org/0000-0003-0462-5385

Jun-ichi Yamaura https://orcid.org/0000-0002-8992-9099

References

[1] Kamihara Y, Watanabe T, Hirano M and Hosono H 2008 Iron-based layered superconductor La[O$_{1-x}$F$_x$]FeAs ($x = 0.05-0.12$) with $T_c = 26$ K *J. Am. Chem. Soc.* **130** 3296

[2] Stewart G R 2011 Superconductivity in iron compounds *Rev. Mod. Phys.* **83** 1589

[3] Hosono H and Matsuishi S 2013 Superconductivity induced by hydrogen anion substitution in 1111-type iron arsenides *Curr. Opin. Solid State Mater. Sci.* **17** 49

[4] Iimura S, Matsuishi S, Sato H, Hanna T, Muraba Y W, Kim S W, Kim J E, Takata M and Hosono H 2013 Two-dome structure in electron-doped iron arsenide superconductors *Nat. Commun.* **3** 943

[5] Iimura S *et al* 2013 Switching of intra-orbital spin excitations in electron-doped iron pnictide superconductors *Phys. Rev. B* **88** 060501(R)

[6] Fujiwara N, TsuTsumi S, Iimura S, Matsuishi S, Hosono H, Yamakawa Y and Kontani H 2013 Detection of antiferromagnetic ordering in heavily doped LaFeAsO$_{1-x}$H$_x$ pnictide superconductors using nuclear-magnetic-resonance techniques *Phys. Rev. Lett.* **111** 097002

[7] Fujiwara N, Iimura S, Matsuishi S, Hosono H, Yamakawa Y and Kontani H 2014 NMR study on a pnictide superconductor LaFeAsO$_{1-x}$H$_x$ in a H-overdoped regime: revival of antiferromagnetic fluctuations *J. Supercond. Nov. Magn.* **27** 933

[8] Hiraishi M *et al* 2014 Bipartite magnetic parent phases in the iron oxypnictide superconductor *Nat. Phys.* **10** 300

[9] Iimura S, Matsuishi S and Hosono H 2016 Heavy electron doping induced antiferromagnetic phase as the parent for the iron oxypnictide superconductor LaFeAsO$_{1-x}$H$_x$ *Phys. Rev. B* **94** 024512

[10] Iimura S and Hosono H 2020 Heavily hydride-ion-doped 1111-type iron-based superconductors: synthesis, physical properties and electronic structure *J. Phys. Soc. Jpn.* **89** 051006

[11] Qureshi N, Drees Y, Werner J, Wurmehl S, Hess C, Klingeler R, Büchner B, Fernández-Díaz M T and Braden M 2010 Crystal and magnetic structure of the oxypnictide superconductor LaFeAsO$_{1-x}$F$_x$: a neutron-diffraction study *Phys. Rev. B* **82** 184521

[12] Sakurai R, Fujiwara N, Kawaguchi N, Yamakawa Y, Kontani H, Iimura S, Matsuishi S and Hosono H 2015 Quantum critical behavior in heavily doped LaFeAsO$_{1-x}$H$_x$ pnictide superconductors analyzed using nuclear magnetic resonance *Phys. Rev. B* **91** 064509

[13] Kuroki K, Onari S, Arita R, Usio H, Tanaka Y, Kontani H and Aoki H 2008 Unconventional pairing originating from the disconnected Fermi surfaces of superconducting LaFeAsO$_{1-x}$F$_x$ *Phys. Rev. Lett.* **101** 087004

[14] Mazin I I, Singh D J, Johannes M D and Du M H 2008 Unconventional superconductivity with a sign reversal in the order parameter of LaFeAsO$_{1-x}$F$_x$ *Phys. Rev. Lett.* **101** 057003

[15] Onari S and Kontani H 2012 Self-consistent vertex correction analysis for iron-based superconductors: mechanism of Coulomb interaction-driven orbital fluctuations *Phys. Rev. Lett.* **109** 137001

[16] Yamakawa Y, Onari S, Kontani H, Fujiwara N, Iimura S and Hosono H 2013 Phase diagram and superconducting states in LaFeAsO$_{1-x}$H$_x$ based on the multiorbital extended Hubbard model *Phys. Rev. B* **88** 041106(R)

[17] Onari S, Yamakawa Y and Kontani H 2014 High-T_c superconductivity near the anion height instability in Fe-based superconductors: analysis of LaFeAsO$_{1-x}$H$_x$ *Phys. Rev. Lett.* **112** 187001

[18] Onari S, Yamakawa Y and Kontani H 2016 Sign-reversing orbital polarization in the nematic phase of FeSe due to the C_2 symmetry breaking in the self-energy *Phys. Rev. Lett.* **116** 227001

[19] Yamakawa Y, Onari S and Kontani H 2016 Nematicity and magnetism in FeSe and other families of Fe-based superconductors *Phys. Rev. X* **6** 021032

[20] Hanna T, Muraba Y, Matsuishi S, Igawa N, Kodama K, Shamoto S and Hosono H 2011 Hydrogen in layered iron arsenides: indirect electron doping to induce superconductivity *Phys. Rev. B* **84** 024521

[21] Matsumoto J, Hanzawa K, Sasase M, Hainl S, Katase T, Hiramatsu H and Hosono H 2019 Superconductivity at 48 K of heavily hydrogen-doped SmFeAsO epitaxial films grown by topotactic chemical reaction using CaH$_2$ *Phys. Rev. Mater.* **3** 103401

[22] Iimura S, Okanishi H, Matsuishi S, Hiraka H, Honda T, Ikeda K, Hansen T C, Otomo T and Hosono H 2017 Large-moment antiferromagnetic order in overdoped high-T_c superconductor ^{154}SmFeAsO$_{1-x}$D$_x$ *Proc. Natl Acad. Sci.* **114** E4354

[23] Hämäläinen K, Siddons D P, Hastings J B and Berman L E 1991 Elimination of the inner-shell lifetime broadening in x-ray-absorption spectroscopy *Phys. Rev. Lett.* **67** 2850

[24] Hämäläinen K, Kao C-C, Hastings J B, Siddons D P, Berman L E, Stojanoff V and Cramer S P 1992 Spin-dependent x-ray absorption of MnO and MnF$_2$ *Phys. Rev. B* **46** 14274

[25] Balédent V, Rullier-Albenque F, Colson D, Ablett J M and Rueff J-P 2015 Electronic properties of BaFe$_2$As$_2$ upon doping and pressure: the prominent role of the as p orbitals *Phys. Rev. Lett.* **114** 177001

[26] Yamaoka H *et al* 2017 Electronic structures and spin states of BaFe$_2$As$_2$ and SrFe$_2$As$_2$ probed by x-ray emission spectroscopy at Fe and as K-absorption edges *Phys. Rev. B* **96** 085129

[27] Yamaoka H 2016 Pressure dependence of the electronic structure of 4f and 3d electron systems studied by x-ray emission spectroscopy *High Press. Res.* **36** 262

[28] Vankó G, Neisius T, Molnár G, Renz F, Kárpáti S, Shukla A and de Groot F M F 2006 Probing the 3d spin momentum with x-ray emission spectroscopy: the case of molecular-spin transitions *J. Phys. Chem. B* **110** 11647

[29] Yamamoto Y *et al* 2016 Origin of pressure-induced superconducting phase in K$_x$Fe$_{2-y}$Se$_2$ studied by synchrotron x-ray diffraction and spectroscopy *Sci. Rep.* **6** 30946

[30] Toyokawa H, Kajiwara K, Sato M, Kawase M, Honma T and Takagaki M 2011 Energy-resolved x-ray imaging method with a counting-type pixel detector *Nucl. Instrum. Method Phys. Res.* A **650** 84

[31] Tsutsumi K 1959 The x-ray non-diagram lines Kβ' of some compounds of the iron group *J. Phys. Soc. Japan* **14** 1696

[32] Tsutsumi K, Nakamori H and Ichikawa K 1976 X-ray Mn $K\beta$ emission spectra of manganese oxides and manganates *Phys. Rev. B* **13** 929

[33] Gretarsson H *et al* 2011 Revealing the dual nature of magnetism in iron pnictides and iron chalcogenides using x-ray emission spectroscopy *Phys. Rev. B* **84** 100509(R)

[34] Gretarsson H *et al* 2013 Spin-state transition in the Fe pnictides *Phys. Rev. Lett.* **110** 047003

[35] See Supplementary information. Carrier-doping dependence of the intensity of the pre-edge peak, method of the IAD analyses, parameters and effect of Udc in the AIM calculations, and detailed Fermi surface mappings are shown.

[36] Hammersley A P, Svensson S O, Hanfland M, Fitch A N and Hausermann D 1996 Two-dimensional detector software: from real detector to idealised image or two-theta scan *High Press. Res.* **14** 235

[37] Momma K and Izumi F 2008 VESTA: a three-dimensional visualization system for electronic and structural analysis *J. Appl. Cryst.* **41** 653

[38] Izumi F and Momma K 2007 Three-Dimensional visualization in powder diffraction *Solid State Phenom.* **130** 15

[39] Westre T E, Kennepohl P, DeWitt J G, Hedman B, Hodgson K O and Solomon E I 1997 A multiplet analysis of Fe *K*-edge 1*s* → 3*d* pre-edge features of iron complexes *J. Am. Chem. Soc.* **119** 6297

[40] Takahashi H, Soeda H, Nukii M, Kawashima C, Nakanishi T, Iimura S, Muraba Y, Matsuishi S and Hosono H 2015 Superconductivity at 52 K in hydrogen-substituted LaFeAsO$_{1-x}$H$_x$ under high pressure *Sci. Rep.* **5** 7829

[41] Takahashi H, Okada H, Igawa K, Kamihara Y, Hirano M and Hosono H 2009 Pressure studies of (La, Sm)FeAsO$_{1-x}$F$_x$ and LaFePO *Phys. C* **469** 413

[42] Takahashi H, Tomita T, Soeda H, Ebata M, Okuma K, Hanna T, Muraba Y, Matsuishi S and Hosono H 2012 High-Pressure Studies for Hydrogen Substituted CaFeAsF$_{1-x}$H$_x$ and SmFeAsO$_{1-x}$H$_x$ *J. Supercond. Nov. Magn.* **25** 1293

[43] Okada H, Igawa K, Takahashi H, Kamihara Y, Hirano M, Hosono H, Matsubayashi K and Uwatoko Y 2008 Superconductivity under high pressure in LaFeAsO *J. Phys. Soc. Japan* **77** 113712

[44] Moon C-Y, Park H, Haule K and Shim J H 2016 Origin of doping-induced suppression and reemergence of magnetism in LaFeAsO$_{1-x}$H$_x$ *J. Phys.: Condens. Matter.* **94** 224511

[45] Mannella N 2014 The magnetic moment enigma in Fe-based high temperature superconductors *J. Phys.: Condens. Matter* **26** 473202

[46] Pelliciari J *et al* 2017 Magnetic moment evolution and spin freezing in doped BaFe$_2$As$_2$ *Sci. Rep.* **7** 8003

[47] Tamatsukuri H *et al* 2018 Gapless magnetic excitation in a heavily electron-doped antiferromagnetic phase of LaFeAsO$_{0.5}$D$_{0.5}$ *Phys. Rev.* B **98** 174415

[48] Kotliar G, Savrasov S Y, Haule K, Oudovenko V S, Parcollet O and Marianetti C A 2006 Electronic structure calculations with dynamical mean-field theory *Rev. Mod. Phys.* **78** 865

[49] Hariki A, Winder M, Uozumi T and Kuneš J 2020 LDA + DMFT approach to resonant inelastic x-ray scattering in correlated materials *Phys. Rev.* B **101** 115130

[50] Hariki A, Winder M and Kuneš J 2018 Continuum charge excitations in high-valence transition-metal oxides revealed by resonant inelastic x-ray scattering *Phys. Rev. Lett.* B **121** 126403

[51] Kuneš J, Leonov I, Kollar M, Byczuk K, Anisimov V I and Vollhardt D 2009 Dynamical mean-field approach to materials with strong electronic correlations *Eur. Phys. J. Spec. Top.* **180** 5

[52] Blaha P, Schwarz K, Madsen G, Kvasnicka D, Luitz J, Laskowski R, Tran F and Marks L D 2018 *WIEN2k, An Augmented Plane Wave + Local Orbitals Program for Calculating Crystal Properties Karlheinz Schwarz Techn* (Austria: Universitat Wien)

[53] Kuneš J, Arita R, Wissgott P, Toschi A, Ikeda H and Held K 2010 Wien2wannier: from linearized augmented plane waves to maximally localized Wannier functions *Comput. Phys. Commun.* **181** 1888

[54] Mostofi A A, Yates J R, Pizzi G, Lee Y-S, Souza I, Vanderbilt D and Marzari N 2014 An updated version of wannier90: a tool for obtaining maximally-localised wannier functions *Comput. Phys. Commun.* **185** 2309

[55] Hariki A, Winder M, Uozumi T and Kuneš J 2017 LDA + DMFT approach to core-level spectroscopy: application to 3*d* transition metal compounds *Phys. Rev.* B **96** 045111

[56] Tonai H, Sasabe N, Uozumi T, Kawamura N and Mizumaki M 2017 Estimation of Ce 4*f* −5*d* interaction by analysis of partial fluorescence yield at the Ce L_3 edge of CeO$_2$ *J. Phys. Soc. Jpn.* **86** 093704

[57] Aichhorn M, Pourovskii L, Vildosola V, Ferrero M, Parcollet O, Miyake T, Georges A and Biermann S 2009 Dynamical mean-field theory within an augmented plane-wave framework: assessing electronic correlations in the iron pnictide LaFeAsO *Phys. Rev.* B **80** 085101

[58] Kuroki K, Usui H, Onari S, Arita R and Aoki H 2009 Pnictogen height as a possible switch between high-T_c nodeless and low-T_c nodal pairings in the iron-based superconductors *Phys. Rev.* B **79** 224511

[59] Kobayashi K *et al* 2016 Pressure effect on iron-based superconductor LaFeAsO$_{1-x}$H$_x$: peculiar response of 1111-type structure *Sci. Rep.* **6** 39646

[60] Iimura S, Muramoto T, Fujitsu S, Matsuishi S and Hosono H 2017 High pressure growth and electron transport properties of superconducting SmFeAsO$_{1-x}$H$_x$ single crystals *J. Asian Ceramic Soc.* **5** 357

[61] Liu R H *et al* 2008 Anomalous transport properties and phase diagram of the FeAs-based SmFeAsO$_{1-x}$F$_x$ superconductors *Phys. Rev. Lett.* **101** 087001

[62] Lee C-H *et al* 2008 Effect of structural parameters on superconductivity in fluorine-free *Ln*FeAsO$_{1-y}$ (*Ln* = La, Nd) *J. Phys. Soc. Japan* **77** 083704

[63] Mizuguchi Y, Hara Y, Deguchi K, Tsuda S, Yamaguchi T, Takeda K, Kotegawa H, Tou H and Takano Y 2010 Anion height dependence of T_c for the Fe-based superconductor *Supercond. Sci. Technol.* **23** 054513

[64] Ni N, Tillman M E, Yan J-Q, Kracher A, Hannahs S T, Bud'ko S L and Canfield P C 2008 Effects of Co substitution on thermodynamic and transport properties and anisotropic H_{c2} in Ba(Fe$_{1-x}$Co$_x$)$_2$As$_2$ single crystals *Phys. Rev.* B **78** 214515

[65] Suzuki K, Usui H, Kuroki K, Iimura S, Sato Y, Matsuishi S and Hosono H 2013 Robust Spin Fluctuations and *s*± Pairing in the Heavily Electron Doped Iron-Based Superconductors *J. Phys. Soc. Japan* **82** 083702